KELT-9 as an Eclipsing Double-lined Spectroscopic Binary: A Unique and Self-consistent Solution to the System

Anusha Pai Asnodkar[1] , Ji Wang (王吉)[1] , B. Scott Gaudi[1] , P. Wilson Cauley[2] , Jason D. Eastman[3] , Ilya Ilyin[4] ,
Klaus Strassmeier[4] , and Thomas Beatty[5]

[1] The Ohio State University, McPherson Laboratory, 140 W. 18th Ave., Columbus, OH 43210, USA; paiasnodkar.1@osu.edu
[2] Laboratory for Atmospheric and Space Physics, University of Colorado Boulder, Boulder, CO 80303, USA
[3] Center for Astrophysics | Harvard & Smithsonian, 60 Garden St., Cambridge, MA 02138, USA
[4] Leibniz-Institut for Astrophysics Potsdam (AIP), An der Sternwarte 16, D14482 Potsdam, Germany
[5] Department of Astronomy and Steward Observatory, University of Arizona, Tucson, AZ 85721, USA

Abstract

Transiting hot Jupiters present a unique opportunity to measure absolute planetary masses due to the magnitude of their radial velocity signals and known orbital inclination. Measuring planet mass is critical to understanding atmospheric dynamics and escape under extreme stellar irradiation. Here we present the ultrahot Jupiter system KELT-9 as a double-lined spectroscopic binary. This allows us to directly and empirically constrain the mass of the star and its planetary companion without reference to any theoretical stellar evolutionary models or empirical stellar scaling relations. Using data from the PEPSI, HARPS-N, and TRES spectrographs across multiple epochs, we apply least-squares deconvolution to measure out-of-transit stellar radial velocities. With the PEPSI and HARPS-N data sets, we measure in-transit planet radial velocities using transmission spectroscopy. By fitting the circular orbital solution that captures these Keplerian motions, we recover a planetary dynamical mass of $2.17 \pm 0.56\, M_J$ and stellar dynamical mass of $2.11 \pm 0.78\, M_\odot$, both of which agree with the discovery paper. Furthermore, we argue that this system, as well as systems like it, are highly overconstrained, providing multiple independent avenues for empirically cross-validating model-independent solutions to the system parameters. We also discuss the implications of this revised mass for studies of atmospheric escape.

Unified Astronomy Thesaurus concepts: Exoplanet astronomy (486); Exoplanet atmospheres (487); Exoplanets (498)

Supporting material: data behind figure

1. Introduction

Absolute mass is a critical but elusive quantity throughout the field of observational astronomy. Most empirical constraints on mass rely on the analysis of the dynamical information of bodies interacting gravitationally, which is not always attainable from 2D projections on the plane of the sky. Stellar eclipsing double-lined spectroscopic binaries (SB2s) are a classic case in which dynamical masses can be directly measured. Spectroscopic observations of two eclipsing stars, and thus stars of known inclination, yield orbital velocities by harnessing the Doppler effect for light. Newton's fundamental law of gravitation can be combined with knowledge of the system's orbital motion to recover the dynamical masses of both stars purely empirically. These measurements calibrate the stellar evolution models that are typically used to determine the masses of stars and, indirectly, the planets they host (Popper 1980; Harmanec 1988; Andersen 1991; Torres et al. 2010; Stevens et al. 2018).

Mass is no less essential for the characterization of transiting planet systems. For example, determining the interior composition of terrestrial planets or measuring atmospheric escape on highly irradiated planets both require knowledge of the planet's mass. Transiting planets and their host stars are in an eclipsing orbital configuration that, in principle, enables a direct measurement of their masses. Transiting hot Jupiters (HJs), in particular, are particularly suitable for this task. Due to their relatively large mass and proximity to their host stars, HJs impart a stronger reflex motion through their gravitational influence on their host stars than other classes of planets. Thus, they are the most accessible class of planets for transit and radial velocity (RV) techniques. The RV signature of the host star can, in principle, be constrained spectroscopically for the most massive and tightly bound HJs, even without high-precision RV instruments.

However, because of their extremely small planet/star flux ratios, most HJ systems are essentially eclipsing single-lined spectroscopic binaries. Such systems do not allow for a unique solution to the masses and radii of the individual objects (Seager & Mallén-Ornelas 2003); rather, there is a 1D degeneracy between the mass and radius of the primary. Thus, any inferences about the mass of a transiting planet require an external constraint on stellar mass, typically from stellar evolution models or empirical scaling relations between the properties of main-sequence stars (Torres et al. 2010; Choi et al. 2016; Dotter 2016; Duck et al. 2021). However, the reliability of the estimates and uncertainties of these semi-empirical measurements has recently been called into question (Tayar et al. 2020). Systematic uncertainties in stellar properties that may deviate from the representative population used to calibrate evolutionary tracks can propagate into an incorrect estimation of planet mass and other planetary parameters. Furthermore, Tayar et al. (2020) showed that current planetary

parameter uncertainties are often disproportionately underestimated relative to the uncertainties on the host star properties from which the planetary parameters are derived. Thus, obtaining masses by purely empirical methods is important because it provides a concrete check on the semiempirical practices that are commonly employed.

If the RV of a transiting planet can also be measured, then the system essentially becomes an eclipsing SB2; thus, an empirical measurement of the system parameters, including the masses of the planet and star, can be made. In this work, we apply the classical techniques used to analyze SB2s to the KELT-9 system (Gaudi et al. 2017) using observations from the the Potsdam Echelle Polarimetric and Spectroscopic Instrument (PEPSI) spectrograph (Strassmeier et al. 2015) on the Large Binocular Telescope (LBT) and the HARPS-N spectrograph on the Telescopio Nazionale Galileo (TNG). KELT-9 b is an ultrahot Jupiter (UHJ) and the hottest known planet to date ($T_{eq} = 4050$ K). The UHJs generally have orbital periods below 3 days, yielding orbital velocities in the range of hundreds of kilometers per second; this is approximately 3 orders of magnitude greater than the orbital velocity of the host star.

Furthermore, the planet's RV can be measured from its atmospheric absorption signature observed during transit. Snellen et al. (2010) is a pioneering work in this field, not only for providing the first measurement of winds on an exoplanet but also for using this technique to empirically constrain the absolute masses of the planet and its host. To simultaneously chart the planet's orbital motion and measure its dayside-to-nightside winds, CO was adopted as a tracer of HD 209458 b's absorption signature. As a result, the Doppler velocity shift of the planet's atmospheric absorption features over the course of a transit spans a broader range of RVs than that of the relatively stationary stellar spectral features. Transmission spectroscopy harnesses this distinction in velocity space to disentangle the planet's spectrum from its host star, allowing for a self-consistent measurement of the planet's absolute mass.

Yan & Henning (2018) adopted this method to measure the masses of KELT-9 b and its host ($M_p = 3.23 \pm 0.94\,M_J$, $M_\star = 3.00 \pm 0.21\,M_\odot$). However, they did not obtain an original measurement of $K_\star$, the stellar orbital velocity; instead, they adopted the value given in Gaudi et al. (2017) measured from TRES stellar spectra. In our work, we utilize the original TRES data in Gaudi et al. (2017), as well as additional RVs from higher-precision spectrographs, PEPSI (LBT) and HARPS-N (TNG), to constrain the dynamical masses of the KELT-9 system through a fully self-contained analysis. In combination with the Hipparcos parallax and spectral energy distribution (SED) fitting in Gaudi et al. (2017) that allow us to constrain KELT-9 b's radius, these observations will provide a purely empirical measurement of the system parameters.

The KELT-9 system is notably overconstrained. A key focus of this work is to emphasize that complementary observations (discussed in Section 5.2) will contribute complete model-independent solutions to the system parameters. All of these constraints can be combined to determine the system parameters to higher accuracy. Improved precision of planetary parameters is critical for science cases pertinent to KELT-9 b, such as atmospheric escape. A tight constraint on mass will enable a more precise understanding of KELT-9 b's atmospheric escape, since the mass-loss rate measurement is dependent on planetary parameters, i.e., mass or surface gravity.

Table 1
Data Sets Used to Measure Stellar RV

Instrument	Night	t_{start} (UTC)	t_{end} (UTC)	N_{obs}
PEPSI	2018-07-03	04:07:34.4	11:16:41.3	82
PEPSI	2019-06-22	05:19:33.7	11:29:06.5	65
PEPSI	2021-06-28	05:55:41.3	11:48:23.5	62[a]
HARPS-N	2017-07-31	20:59:04.0	05:19:10.0	49
HARPS-N	2018-07-20	21:20:24.0	05:09:58.0	46
TRES	2014–2016			60[a]

Notes. Columns provide the name of the instrument, the date of the starting observation, the start and end times of the observation, and the number of observations.
[a] Out-of-transit only.

Like Snellen et al. (2010), we use a fully self-consistent technique analogous to the study of SB2s to obtain the absolute masses of the KELT-9 system. In Section 2, we describe our new data sets from the PEPSI spectrograph, as well as the archival HARPS-N observations we use in our analysis. In Section 3, we outline the techniques we use to recover stellar and planetary orbital velocities and subsequently determine the absolute masses of the planet and star. In Section 4, we report our resulting mass constraints and compare our findings with previous literature. In Section 5, we discuss the ways in which the properties of the KELT-9 system are potentially empirically overconstrained. We consider contributions from current and future complementary observations. When combined, we argue that these will lead to a complete solution of system parameters. We also discuss the implications for atmospheric escape. Finally, we present our conclusions in Section 6.

2. Observations

We observed two transits of KELT-9 b with the high-resolution echelle spectrograph PEPSI (Strassmeier et al. 2015) on the LBT (two 8.4 m mirrors, effective aperture of 11.8 m) in Arizona (see Table 1 for the specific nights of observations). PEPSI has a blue arm (nominally 3830–5440 Å) and a red arm (nominally 5440–9070 Å) with six cross-dispersers for full optical coverage. In this work, we use high-resolution data from the blue arm taken with cross-disperser 3 (∼4750–5430 Å, $R = 50,000$) exclusively because of negligible telluric contamination (Cauley et al. 2019). The PEPSI pipeline produces wavelength-calibrated 1D spectra of each order, which are then continuum normalized, corrected for solar barycentric motion, and stitched into a single 1D spectral vector.

Our PEPSI data set taken on 2018 July 3 (hereafter PEPSI 2018) was originally presented with an analysis of KELT-9 b's Balmer and metal lines in Cauley et al. (2019). In the blue arm, the spectra were taken with exposure times between 220 and 387 s (depending on fluctuations in observing conditions) to approximately maintain a constant signal-to-noise ratio (S/N) of 210 in the continuum; in practice, the S/N ranged between 182 and 219 across observations. Additionally, we present a new data set taken on 2019 June 22 (hereafter PEPSI 2019) for which observations began during the transit. The exposure times of the blue arm spectra were between 214 and 270 s with continuum S/Ns ranging between 286 and 321.

We utilized two archival HARPS-N data sets from the Italian Center for Astronomical Archives (IA2) Facility to increase the number of stellar RV samples for our measurement of the host star's orbital motion. HARPS-N is a high-resolution ($R \sim$

Table 2
KELT-9 System Parameters

Parameter	Units	Symbol	Value	Source
Stellar Parameters				
Stellar mass	$M_\odot$	$M_\star$	$2.52^{+0.25}_{-0.20}$	Gaudi et al. (2017)
Stellar radius	$R_\odot$	$R_\star$	$2.362^{+0.075}_{-0.063}$	Gaudi et al. (2017)
Stellar density	g cm^{-3}	$\rho_\star$	0.2702 ± 0.0029	Gaudi et al. (2017)
Effective temperature	K	$T_{\rm eff}$	$10{,}170 \pm 450$	Gaudi et al. (2017)
Projected rotational velocity	km s^{-1}	$v \sin i$	111.4 ± 1.3	Gaudi et al. (2017)
Planetary Parameters				
Planet mass	$M_{\rm J}$	$m_{\rm p}$	2.88 ± 0.84	Gaudi et al. (2017)
Planet radius	$R_{\rm J}$	$R_{\rm p}$	$1.891^{+0.061}_{-0.053}$	Gaudi et al. (2017)
Semimajor axis	au	a	$0.03462^{+0.00110}_{-0.00093}$	Gaudi et al. (2017)
Eccentricity		ε	0	Gaudi et al. (2017)
Spin–orbit alignment	deg	λ	-84.8 ± 1.4	Gaudi et al. (2017)
Orbital inclination	deg	$i_{\rm orbit}$	86.79 ± 0.25	Gaudi et al. (2017)
Ephemeris				
Midtransit time	BJD$_{\rm TDB}$	T_0	$2{,}458{,}566.436560 \pm 0.000048$	This work
Time of secondary eclipse	BJD$_{\rm TDB}$	T_S	$2{,}458{,}584.950546 \pm 0.000048$	This work
Orbital period	days	P	$1.48111890 \pm 0.00000016$	This work
Ingress/egress transit duration	days	τ	$0.012808^{+0.000027}_{-0.000026}$	This work
Total transit duration	days	T_{14}	0.15949 ± 0.00011	This work

Note. General stellar and planetary parameters from the discovery paper, as well as updated measurements of the orbital configuration and ephemerides from this work.

115,000) optical spectrograph (wavelength range between 3874 and 6909 Å) on the TNG in La Palma, Spain. The first night of HARPS-N observations is from 2017 July 31 (hereafter HARPS-N 2017), and the other is from 2018 July 20 (hereafter HARPS-N 2018); both were originally presented in Hoeijmakers et al. (2019). The S/N of a given observation in these data sets ranges between 35 and 140, depending on the order, at exposure times of 600 s. We retrieved the 1D, order-stitched spectra from the IA2 Archive Facility.

Three of the data sets (PEPSI 2018, HARPS-N 2017, and HARPS-N 2018) include observations taken immediately before, during, and immediately after transit. PEPSI 2019 only includes observations during and immediately after transit. We converted all observation timings from their respective timing systems (PEPSI times are provided in both JD$_{\rm UTC}$ and HJD$_{\rm UTC}$; HARPS-N times are provided in MJD$_{\rm UTC}$) to BJD$_{\rm TDB}$ using the Time Utilities[6] online software tool (Eastman 2012) to make them comparable with our revised ephemerides of the KELT-9 system (see Table 2). This is a crucial step for precision RV measurements (Eastman et al. 2010), especially of atmospheric dynamics. The JD$_{\rm UTC}$-to-BJD$_{\rm TDB}$ conversion (see Eastman et al. 2010 for a detailed description of the difference between JD$_{\rm UTC}$ and BJD$_{\rm TDB}$) is not accounted for in previous literature, e.g., Cauley et al. (2019), and yields a difference of up to 4.4 minutes in our PEPSI data sets. Note that the discovery paper (Gaudi et al. 2017) ephemeris, which is commonly adopted in KELT-9 b literature, is also in the BJD$_{\rm TDB}$ timing system.

3. Methods

3.1. Stellar Orbital Properties

To measure the dynamical mass of KELT-9 b, we need to know the orbital properties of the planet and its host star. We first recover the out-of-transit stellar velocities by least-squares deconvolution (LSD) of the stellar spectra across our data sets

to fit for the stellar orbital velocity and systemic RV as measured by each instrument.

3.1.1. LSD of Stellar Line Profiles

In subsequent analysis, $K_\star$ (stellar RV semiamplitude) and $v_{{\rm sys},\,i}$ (systemic velocity measured by instrument i) are crucial values. The systemic RV of the KELT-9 system has been a point of controversy in previous literature (Gaudi et al. 2017; Borsa et al. 2019; Hoeijmakers et al. 2019); see Table 3 for a compilation of the different literature values. The standard procedure to recover stellar velocities is to centroid the cross-correlation function (CCF) profiles of the observations, where the CCF is the observed stellar spectra cross-correlated with a template spectrum corresponding to the star's effective temperature, with a Gaussian fit. This method becomes increasingly imprecise for fast rotators due to significant rotational broadening.

Since KELT-9 is a rapidly rotating A0 star ($v \sin i =$ 111.4 km s^{-1}), we recover our own measurements of $K_\star$ and $v_{{\rm sys},\,i}$ by performing LSD on our time-resolved stellar spectra to recover the rotational broadening kernel (with in-transit observations affected by the Rossiter–McLaughlin effect, RME) of the star at each time of observation. The LSD procedure allows for tunable regularization of the recovered line profile, a feature that cross-correlation does not accomplish. The rotational kernel is centered on the star's RV at the time of observation, which we can fit for using an analytical kernel defined according to the star's $v \sin i$. These velocities over time can be fit with the orbital RV equation to determine $K_\star$ and $v_{{\rm sys},\,i}$. This procedure was previously adopted in Borsa et al. (2019).

For the first step, we refer to the LSD procedure provided in Kochukhov et al. (2010) with the modification for regularization given in Wang et al. (2017). In our application of this technique, $\mathbf{Y}^0$ is a logarithmically sampled, n-element vector of the observed rotationally broadened stellar spectrum, and $\mathbf{F}$ is a template stellar spectrum of the corresponding $T_{\rm eff}$. Here $\mathbf{F}$

---

6 https://astroutils.astronomy.osu.edu/time/utc2bjd.html

Table 3
KELT-9 Revised System Parameters

Parameter	Units	Value	Source
$v_{sys,\text{PEPSI}}$	km s^{-1}	-17.86 ± 0.044	This work
$v_{sys,\text{HARPS-N}}$	km s^{-1}	-17.15 ± 0.11	This work
		-17.74 ± 0.11	Hoeijmakers et al. (2019)
		-19.819 ± 0.024	Borsa et al. (2019)
$v_{sys,\text{TRES}}$	km s^{-1}	-18.97 ± 0.12	This work
		-20.567 ± 0.1	Gaudi et al. (2017)
$K_\star$	km s^{-1}	0.23 ± 0.060	This work
		0.276 ± 0.079	Gaudi et al. (2017)
		0.293 ± 0.032	Borsa et al. (2019)
K_p	km s^{-1}	$239.07^{+5.83}_{-5.79}$	This work
		$268.7^{+6.2}_{-6.4}$	Yan & Henning (2018)
		234.24 ± 0.90	Hoeijmakers et al. (2019)
		241.5^{+3}_{-2}	Pino et al. 2020
$M_\star$	$M_\odot$	2.11 ± 0.78	This work
		$2.52^{+0.25}_{-0.20}$	Gaudi et al. (2017)
		3.00 ± 0.21	Yan & Henning (2018)
		1.978 ± 0.023	Hoeijmakers et al. (2019)
m_p	M_J	2.17 ± 0.56	This work
		2.88 ± 0.84	Gaudi et al. (2017)
		3.23 ± 0.94	Yan & Henning (2018)
		2.44 ± 0.70	Hoeijmakers et al. (2019)
$\rho_\star$	g cm^{-3}	0.29 ± 0.17	This work
		0.2702 ± 0.0029	Gaudi et al. (2017)

has the same logarithmic wavelength sampling as the observed spectrum but is not rotationally broadened. We generate F by inputting the VALD3 line list for a $T_{\text{eff}} = 10{,}170$ K star into the IDL software `Spectroscopy Made Easy` (SME) at 21 different limb-darkening angles (Valenti & Piskunov 1996, 2012). We treat the stellar disk as a pixelated grid of $0.01R_\star \times 0.01R_\star$ cells to (1) interpolate in the limb-darkening angle to generate the corresponding spectrum for each cell, (2) add up the spectra of each cell, and (3) continuum normalize to generate the disk-integrated stellar spectrum F.

The deconvolution process recovers the rotational broadening kernel that transforms F into Y^0. It can be described through matrix multiplication of (1) the cross-correlation between a line mask, M, and the observed spectrum and (2) the inverse of the autocorrelation of the line mask modified by regularization. This is mathematically represented by the following equation (analogous to Equation (1) in Wang et al. 2017, assuming homoscedasticity):

$$Z(v_i) = (M^{\text{T}} \cdot M + \Lambda R)^{-1} \cdot M^{\text{T}} \cdot Y^0, \qquad (1)$$

where $Z(v_i)$ is the m-element vector of the deconvolved line profile (our output of interest), and M is an $n \times m$ line mask constructed by expanding the template spectrum into its corresponding Toeplitz matrix; we adopt the definition provided in Donati et al. (1997). For regularization, Λ is a regularization parameter, and R is the $m \times m$ matrix of first-order Tikhonov regularization; we adopt Equation (16) in Donatelli & Reichel (2014) for the form of R. The velocities v_i corresponding to the elements in the line profile $Z(v_i)$ are determined by the wavelength shift of each row in the M matrix relative to the template spectrum and should be linearly spaced, since we constructed a template spectrum that is logarithmically spaced in wavelength.

We apply this deconvolution algorithm to all of our out-of-transit observations, since the in-transit kernels contain a deficiency in the rotationally broadened line profile due to the RME. As the planet transits, it blocks a region of the stellar disk, and the contribution from this portion of the stellar disk is not added to the integrated stellar disk spectrum. This manifests as a deficiency in the rotational broadening kernel at the RV of that portion of the stellar disk based on stellar rotation. We pooled together our PEPSI data with publicly available HARPS-N data and TRES data from the discovery paper (Gaudi et al. 2017) to increase our sample size and out-of-transit coverage (see Table 1).

3.1.2. Analytic Rotational Kernel Fit to Stellar Line Profiles

Upon generating the observational line profiles, we fit each one with an analytic rotational kernel model to determine their centers and recover an orbital RV curve of the star. We use the analytical expression for a rotational broadening kernel given in Gray (2005; Equation (18.14)), which is adapted for our application as follows:

$$G(v_i, t) = c_1 \left[1 - \left(\frac{v_i - v_\star(t)}{v \sin i} \right)^2 \right]^{1/2} + c_2 \left[1 - \left(\frac{v_i - v_\star(t)}{v \sin i} \right)^2 \right], \qquad (2)$$

where $G(v_i)$ is the analytical rotational kernel defined over a range of velocities v_i, $v_\star(t)$ is the centroid of the rotational kernel and represents the RV of the star at the time t of a given observation, $v \sin i$ is the width of the kernel and represents the sky-projected rotational velocity of the star (we used the value from Gaudi et al. 2017 of 111.4 km s^{-1} to ensure that the same value was used across observations; the residuals in the left panel of Figure 1 suggest that this value sufficiently matches the data), and c_1 and c_2 are constants defined in terms of $v \sin i$ and the linear limb-darkening coefficient of the star, ϵ, as

$$c_1 = \frac{2(1 - \epsilon)}{\pi v \sin i (1 - \epsilon/3)} \qquad (3)$$

and

$$c_2 = \frac{\epsilon}{2v \sin i (1 - \epsilon/3)}. \qquad (4)$$

For each observation, we apply least-squares fitting from `scipy`[7] (Virtanen et al. 2020) to determine the best-fit values of $v_\star$, ϵ, a multiplicative scaling factor (rescales the analytical kernel to match the scaling of the empirical deconvolved line profiles), and an additive offset (the empirical deconvolved line profiles may not have a baseline centered at zero due to a lack of flux conservation between the template and observed spectra). Of these parameters, we are most interested in $v_\star$, which provides measurements of the star's RV over time. We estimated the RV errors by bootstrapping the residuals of the flat region of the deconvolved kernel ($|$velocity$| > v \sin i$ in the left panel of Figure 1), adding the samples to the best-fit model kernel, and refitting the line profile. We repeated this bootstrapping procedure to obtain 1000 resampled values of $v_\star$ for each observation and took the 16th and 84th percentile samples as the $\pm 1\sigma$ errors on the best-fit $v_\star$.

---

[7] https://www.scipy.org/index.html
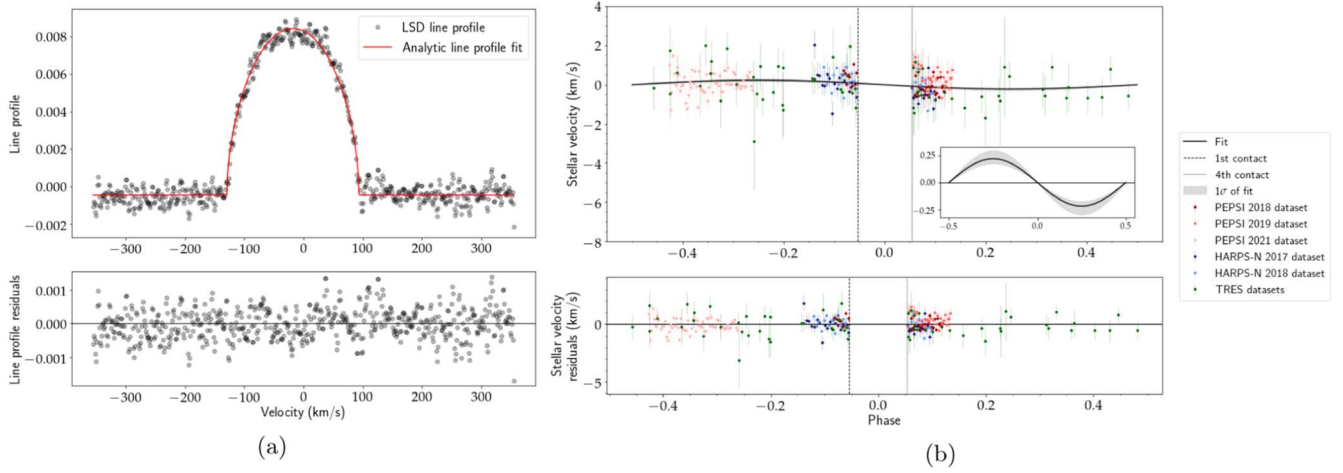
Figure 1. (a) Example of an LSD of a stellar line profile with an analytic rotational kernel fit to a centroid stellar RV. (b) Stellar RV curve of the KELT-9 system derived from fitting a circular orbital solution to the out-of-transit stellar RVs. The data points are shifted by the best-fit systemic velocities of their corresponding data sets. The inset in the top right panel zooms in on the range of velocities along the *y*-axis spanned by the best-fit orbital solution.

(The data used to create this figure are available.)

We also tested fixing the limb-darkening parameter to $\epsilon = 0.3356$ based on the stellar parameters that best describe KELT-9 in the limb-darkening tables provided by Claret (2017). Upon refitting the rotational broadening profiles, we find that the differences in the recovered stellar RVs when ϵ is fixed are not significant enough to affect the resulting stellar orbital parameters (discussed in Section 3.1.3) within the errors.

3.1.3. Stellar Orbital Solution

To obtain the stellar orbital parameters, we fit a circular orbital RV solution to our time-resolved measurements of stellar velocity, which have the following form:

$$v_\star(t) = K_\star \sin\left(\frac{t - t_0}{p}\right) + v_{\text{sys},i}, \qquad (5)$$

where $v_\star(t)$ is the stellar RV as a function of time, $K_\star$ is the stellar RV semiamplitude (stellar orbital velocity for a circular orbit), t_0 is the midtransit time, P is the orbital period, and $v_{\text{sys},\,i}$ is the systemic velocity of a given instrument. We apply the Markov Chain Monte Carlo (MCMC) method to sample the parameter space using the emcee[8] code (Foreman-Mackey et al. 2013). We fit three common parameters that apply across all data sets: midtransit time ephemeris (t_0), period (p), and stellar RV semiamplitude (K_p). We also fit three individual systemic velocities that singly apply to their corresponding data sets: $v_{\text{sys, PEPSI}}$, $v_{\text{sys, HARPS-N}}$, and $v_{\text{sys, TRES}}$. Assuming a fixed $v_{\text{sys},\,i}$ across all data sets for a given instrument is valid, since all three instruments are wavelength-calibrated against a ThAr reference, which guarantees instrumental RV stability.

We apply linearly uniform priors on all model parameters except t_0 and p, for which we use Gaussian priors centered on the midtransit time ephemeris and period, respectively, as provided in Table 2 (T_0 and P) with their corresponding errors as the standard deviations of the Gaussians. See Table 4 for

priors. The priors T_0 and P are updated ephemerides for the KELT-9 b system refitted with EXOFASTv2 (Eastman et al. 2019) to include recent TESS observations (Ricker et al. 2014) in addition to the follow-up light curves and TRES RVs from the discovery paper. The updated ephemerides are critical for this analysis, since the observations span multiple years; the error propagation using the original ephemerides can be as large as 4.8 minutes for the PEPSI 2019 data set. Introducing the TESS 2019 data light curves to the global fit improves the precision of the ephemerides and eliminates the issue of "stale" ephemerides by spanning a broad temporal baseline.

We evaluate the goodness of fit for a given model using the log likelihood $\ln \mathcal{L} \equiv -\frac{\chi^2}{2}$. Here χ^2 is the statistical χ^2, defined as $\chi^2 = \sum\left(\frac{\text{data} - \text{model}}{\text{data errors}}\right)^2$, of the model. To ensure that the log prior is on a comparable scale as the log likelihood, we scale the priors by the number of elements in the observed stellar RV curve before summing the log prior and log likelihood in the log posterior. We run the emcee sampler with 10 walkers until the chain length is at least 100 times the estimated autocorrelation time and the estimated autocorrelation time has changed by less than 1%, checking every 500 steps. Under these criteria, the posterior distributions of all parameters appear sufficiently Gaussian or converged. See the right panel of Figure 1 for the observed and best-fit model stellar RV curve. Table 3 reports the fitted systemic velocities and stellar RV semiamplitude from this analysis.

3.2. Planet Orbital Properties

To obtain the orbital properties of the planet, we generate transmission spectra that feature the planet's atmospheric absorption track during transit, as well as secondary effects due to the geometry of the planet's transit across a nonuniform stellar disk. We simultaneously model both of these signatures and apply a Bayesian framework for fitting the data with MCMC; the most relevant output of this procedure is the orbital velocity of the planet, K_p, which we will use later in this work to constrain the dynamical mass of the planet.

---

[8] https://emcee.readthedocs.io/en/stable/

Table 4
Stellar Orbital Solution MCMC Priors

Parameter	Units	Prior
t_0	BJD_{TDB}	Gaussian prior Center: 2,458,566.436560 Width: 0.000048
p	days	Gaussian prior Center: 1.48111890 Width: 0.00000016
$K_\star$	km s^{-1}	Linearly uniform prior Lower bound: −1 Upper bound: 0
$v_{sys,\ PEPSI}$	km s^{-1}	Linearly uniform prior Lower bound: −100 Upper bound: 0
$v_{sys,\ HARPS-N}$	km s^{-1}	Linearly uniform prior Lower bound: −100 Upper bound: 0
$v_{sys,\ TRES}$	km s^{-1}	Linearly uniform prior Lower bound: −50 Upper bound: 50

3.2.1. Transmission Spectrum Construction

We constrain the RV semiamplitude of the planet, K_p, and global dayside-to-nightside winds, v_{wind}, from a line-by-line analysis of the atmospheric absorption signature seen in our transmission spectra of KELT-9 b from PEPSI. To extract the planet's atmospheric absorption signature, we chose to focus on six Fe II lines in the wavelength range between 4915 and 5400 Å to avoid telluric contamination and broad features such as the Hβ line around 4861.4 Å. The outputs from the PEPSI pipeline are continuum-normalized stellar spectra, which we interpolate onto the same logarithmically spaced wavelength grid constructed such that absorption features are as well sampled as they are by the original wavelength grid. This enables uniform spacing in velocity across all observations. We constructed an empirical combined stellar spectrum by taking the average of the out-of-transit spectra, which were identified using updated ephemerides of the KELT-9 b system (see Table 2). To remove the stellar component, we divide all spectra by the combined stellar spectrum. The residual transmission spectra contain the planet's signature, as well as secondary geometric effects caused by the RME (McLaughlin 1924; Rossiter 1924; Queloz et al. 2000; Ohta et al. 2005; Gaudi & Winn 2007) and center-to-limb variation (CLV; Stenflo 2015; Yan et al. 2015; Yan & Henning 2018), which are both consequences of nonuniformity across the stellar disk (see the Doppler shadow in Figure 2, a by-product of RME). These features are distinguishable because they span different regions of velocity space and contribute opposing signs to the flux map.

Upon inspection of our transmission spectra in the wavelength range between 4915 and 5400 Å for planet atmospheric signatures, we noticed that Fe II lines presented the strongest atomic absorption signatures (apart from Balmer lines, which are significantly broader as well). Previous studies of KELT-9 b's atmosphere with transmission spectroscopy revealed a diverse array of Balmer lines ranging from Hα to Hζ (Yan & Henning 2018; Cauley et al. 2019; Wyttenbach et al. 2020). Due to the extreme heating of KELT-9 b's atmosphere, traces of heavy metals, both neutral and ionized, have also been
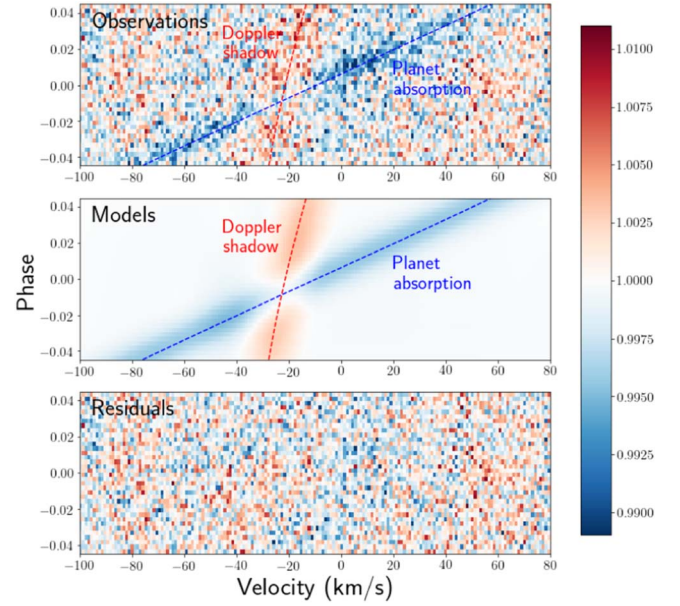
Figure 2. A 2D map of transmission spectra over the course of KELT-9 b's transit for the PEPSI 2018 data set; the blue track is formed by the planet's atmospheric absorption, while the red track is the Doppler shadow from the RME. The top panel displays fully in-transit observations. The middle panel shows the best-fit model from MCMC sampling, with the Doppler shadow and CLV determined from numerical modeling of the planet's transit using SME stellar models, while the planet absorption track is a uniform Gaussian signal shifted in velocity according to the best-fit orbital motion of the planet, systemic velocity, and best-fit dayside-to-nightside winds. The bottom panel shows the residuals (data–model).

found either by directly investigating the atomic absorption lines (Cauley et al. 2019) or by harnessing the cross-correlation technique to boost the absorption signal (Hoeijmakers et al. 2019). Like Cauley et al. (2019), we find that the strongest metal features in our selected wavelength range are produced by Fe II; although signatures of Fe I, Ti II, and Mg I can be observed without cross-correlation in our PEPSI data sets, we have chosen to focus on the Fe II lines to ensure that our measurement of K_p is reliably derived from narrow absorption features that have the highest S/N.

For each of our six selected Fe II lines, we focus on a tightly restricted span of wavelengths that completely encapsulates the planet absorption and Doppler shadow signatures for the observations that are fully in transit (between second and third contact). Thus, we have a flux map of the fully in-transit observations for each Fe II line. Wavelength is on the x-axis, and orbital phase is on the y-axis. The values in the map correspond to the continuum-normalized transmission spectrum fluxes during transit.

We then generate a template spectrum of the Fe II species in the planet's atmosphere using `petitRADTRANS`[9] (Mollière et al. 2019), a radiative transfer code for modeling transmission and emission spectra of planetary atmospheres. We note that at the time of writing, the Fe II opacities used by `petitRAD-TRANS` are in air, unlike most other species, which are given in vacuum; hence, we did not need to perform any wavelength correction to match the template spectrum wavelengths with our observations. The planetary parameters we adopt for R_p, $R_\star$, m_p, $\log g_p$, and T_{eq} are provided in Table 2. Additional parameters that are necessary for generating a transmission

---

[9] https://petitradtrans.readthedocs.io/en/latest/

Table 5
Additional `petitRADTRANS` Parameter Inputs

Parameter	Units	Value
Equilibrium temperature	K	4050
Internal temperature	K	100
Pressure range	bars	10^{-10}–10^{2}
Reference pressure	bars	10^{-9}
Infrared atmospheric opacity		0.01
Ratio between optical and IR opacity		0.4
Abundances		
Fe II		0.00125
H_2		0.748
He		0.250

spectrum in `petitRADTRANS` are available in Table 5. Abundances were chosen to be close to solar (Palme et al. 2014), while the pressure structure was constructed to encompass the region of the atmosphere that most strongly affects line formation in transmission spectra. It is not essential to accurately model the specific shape of lines in the resulting template spectrum of the planet's atmosphere, as the line centers are the most relevant quantity for our analysis of the planet's orbital velocity through the Doppler effect.

With the wavelengths of the Fe II line centers from the template spectrum, we can convert our flux maps from wavelength space to velocity space with the simplified Doppler effect for nonrelativistic speeds,

$$v \approx c \frac{\lambda - \lambda_0}{\lambda_0}, \qquad (6)$$

where λ_0 is the line center corresponding to the Fe II line that generates the absorption feature in a given flux map. We shift our flux maps to the rest frame of the star–planet system by subtracting the systemic velocity calculated in Section 3.1.3 from the velocity grid of each flux map. The resulting flux maps of each Fe II line are presented in Figure 3.

3.2.2. Secondary Effect Modeling

We follow the numerical approach to modeling RME and CLV presented in Casasayas-Barris et al. (2020; originally presented in Yan et al. 2015, 2017, modified for planet radius interpolation in Casasayas-Barris et al. 2020). We obtain line lists corresponding to the properties of the KELT-9 host star from VALD3 (Pakhomov et al. 2017). Known stellar properties from Gaudi et al. (2017) are input into the IDL software `SME` to model the host star spectrum using the VALD3 (Pakhomov et al. 2017) line lists at 21 different limb-darkening angles (Valenti & Piskunov 1996, 2012). We model the planet's transit across a pixelated grid of $0.01R_\star \times 0.01R_\star$ cells that make up the stellar disk. The sky-projected position of the planet is computed according to Equations (7) and (8), which are analogous to Equations (7), (8), and (10) in Collier Cameron et al. (2010; with the sign error in their Equation (10) corrected; this error was originally noted in Eastman et al. 2019):

$$x = x_p \cos \lambda + y_p \sin \lambda, \qquad (7)$$

$$y = -x_p \sin \lambda + y_p \cos \lambda, \qquad (8)$$

where

$$x_p = a \sin \frac{2\pi(t - t_0)}{P}, \qquad (9)$$

$$y_p = a \cos \frac{2\pi(t - t_0)}{P} \cos i_{orbit}. \qquad (10)$$

In Equations (7)–(10), λ is the sky-projected obliquity, a is the semimajor axis of the planet's orbit, t_0 is the midtransit time, P is the orbital period of the planet, i_{orbit} is the orbital inclination of the planet, and t is the time of a given observation; the system parameters related to these equations can be found in Table 2. We generate a grid of orbital phases that Nyquist samples the phases of the observations, and for each phase in the grid, we identify which cells are unobscured by the planet's transit. We interpolate in the limb-darkening angle to generate a spectrum for each unobscured cell and shift the spectrum in velocity according to the cell's RV as determined by its location on the stellar disk and the $v \sin i$ of the star. Then we add up the velocity-shifted spectra of each unobscured cell, continuum normalize, and divide by the out-of-transit model spectrum (the sum of the spectra of all cells interpolated in the limb-darkening angle and shifted in RV, then continuum normalized) to generate the disk-integrated transmission spectrum (excluding the planet's absorption signature) for each phase. In this manner, we produce a 2D map of spectra over different orbital phases that encapsulate both the RME and the CLV that perturb the transmission spectra during the planet's transit. We generate a grid of such models for a range of planet radii spanning $0.7R_p < R < 2.5R_p$, as done in Casasayas-Barris et al. (2020).
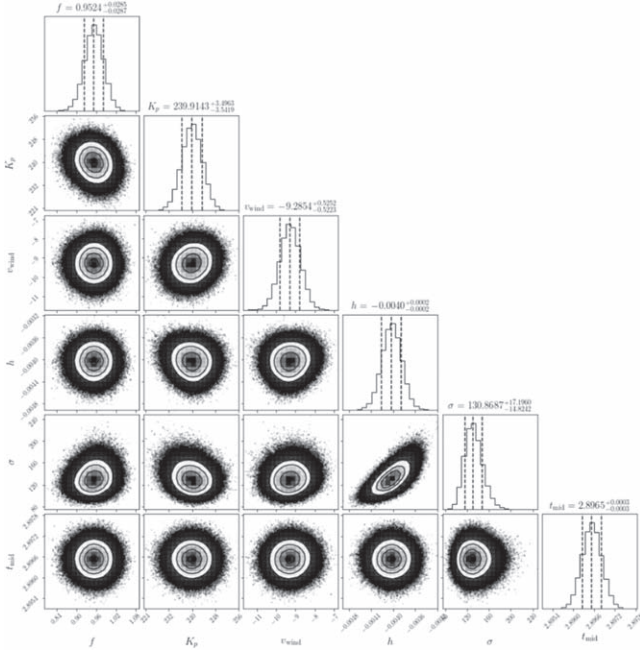
3.2.3. Line-by-line Analysis of Fe II Lines

We apply a procedure analogous to the MCMC fitting of the observed transmission spectra presented in Casasayas-Barris et al. (2020) using `emcee`. To avoid additional asymmetries and velocity offsets from equatorial jets and rotation, we exclude observations during ingress and egress and instead focus on fully in-transit observations such that any velocity shifts from atmospheric dynamics can be treated as a constant blueshifted offset from dayside-to-nightside winds. We fit for the following free parameters: the effective planet radius factor in RME/CLV modeling (f), the RV semiamplitude of the planet (K_p), the RV of the terminator-averaged atmosphere in the planet's rest frame (v_{wind}), the contrast of the planet's Gaussian atmospheric absorption profile (h), the standard deviation of the planet's Gaussian atmospheric absorption profile (σ), and the midtransit time (t_0). See Figure 4 for a sample corner plot.

We generate model flux maps according to the input parameters as follows. The parameter f corresponds to a model map of the RME and CLV effect from the grid of models generated in Section 3.2.2 by interpolating between models in planet radius according to the value of f, then interpolating the resulting map in wavelength (then converted to velocity according to the reference Fe II line of the data map being fitted and applying Equation (6)) and orbital phase to match the observations, i.e., the single line data maps generated in Section 3.2.1.
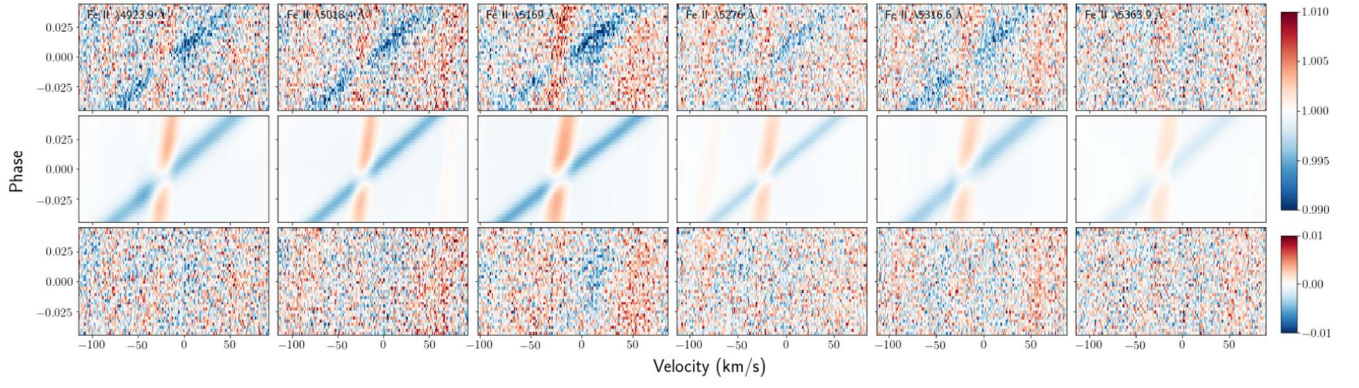
Figure 3. Expanded version of Figure 2 displaying the six Fe II absorption lines chosen for fitting K_p (PEPSI 2018 data set).

Figure 4. Example of a corner plot from MCMC fitting of the Fe II $\lambda4923.9$ flux map.

Table 6
Planet Orbital Solution MCMC Priors (Same for Both Line-by-line and Cross-correlation Analysis)

Parameter	Units	Prior
f		Uniform prior
		Lower bound: 0.7
		Upper bound: 2.5
K_p	km s^{-1}	Uniform prior
		Lower bound: 100
		Upper bound: 350
v_{wind}	km s^{-1}	Uniform prior
		Lower bound: –50
		Upper bound: 50
h		Uniform prior
		Lower bound: –1
		Upper bound: 0
σ	velocity pixels	Uniform prior
		Lower bound: 0
		Upper bound: 1000
t_0	BJD$_{\mathrm{TDB}}$	Gaussian prior
		Center: 2,458,566.436560 propagated to epoch of data set
		Width: 0.000048 propagated (according to error on orbital period) to epoch of data set

Recall that t_0 is a free parameter in this fitting procedure (this is not done in Casasayas-Barris et al. 2020 or Yan et al. 2017); we have added this extra free parameter so that we can include the uncertainty of midtransit time, which is strongly correlated with the parameter v_{wind}, in our analysis. We inject a Gaussian signal into our model maps that varies in velocity with time but remains constant in amplitude and width to represent the planet's absorption signature. The parameters K_p, v_{wind}, and t_0 determine the center of the planet's atmospheric absorption signal as a function of orbital phase (which is, once again, dependent on the free parameter t_0) in our models as follows:

$$v_p(\phi) = K_p \sin(2\pi\phi) + v_{\mathrm{wind}}. \qquad (11)$$

The strength and width of the planet's atmospheric absorption signal is dependent on the free parameters h and σ, resulting in the following form for the planet's absorption signature as a function of the RVs v and orbital phases ϕ that correspond with the observed flux maps:

$$T_v(\phi) = 1 + h e^{\frac{v - v_p(\phi)}{2\sigma}}. \qquad (12)$$

This is analogous to Equation (1) in Yan & Henning (2018).

We adopt a Bayesian framework for sampling the parameter space with MCMC. We apply linearly uniform priors on all model parameters except t_0, for which we use a Gaussian prior centered on the midtransit time value provided in Table 2 (T_0, propagated to the epoch of the corresponding data set being fitted) with a standard deviation that matches the propagated midtransit time error. See Table 6 for priors. As before, we use $-\frac{\chi^2}{2}$ as the log likelihood of a given model and scale the priors by the number of elements in the observed flux map (which should be the same as the number of elements in the model flux map) before summing the log prior and log likelihood in the log posterior. We run the emcee sampler with 10 walkers until the estimated autocorrelation time is 1.5% of the chain length and the estimated autocorrelation time has changed by less than 1%, checking every 500 steps. Under these criteria, the posterior distributions of all parameters appear sufficiently Gaussian or converged.

The main goal of the model fitting for the purposes of this work is to recover a value for K_p; v_{wind}, or dayside-to-nightside winds, will be the topic of a future work. The last 25% of the samples are extracted from the 10 walkers for a given Fe II line and aggregated into one chain for each Fe II line. We weight

each sample from all six chains according to the S/N of the Fe II line flux map it corresponds to. The signal of a given flux map is the 50th percentile sample of h in the flux map's chain. Noise is the standard deviation of the residuals, i.e., the best-fit model subtracted from the flux map, where the best-fit model is a model generated by the 50th percentile parameters from the chain of the flux map. We combine the weighted chains to determine a representative value for the quantity of interest. We recover a representative value of K_p by taking the S/N-weighted 50th percentile sample across all chains. The lower and upper 1σ values are the S/N-weighted 16th and 84th percentile samples, respectively. See Figure 7 for the best-fit K_p for each line analyzed in both PEPSI data sets, as well as the representative value (dashed black line) from combining the MCMC analysis of all lines. Literature values are provided for comparison.

3.2.4. Planet Orbital Properties: Cross-correlation Analysis of Fe II Lines

Since the S/N for the HARPS-N data is significantly lower than that for the PEPSI data, individual lines are noisier in the HARPS-N observations. Cross-correlation is a technique that can boost the S/N by adding up contributions from matching signals between an observed and template spectrum across multiple features. For comparison with the publicly available archival HARPS-N observations of KELT-9 b, we cross-correlate our transmission spectra with a template Fe II template spectrum (we will call it $f(\lambda)$ and the observed flux map $F(\lambda, \phi)$). We cross-correlate our PEPSI and HARPS-N transmission spectra between 4950 and 5400 Å (avoiding the broad Hβ feature) with the Fe II template generated in petitRADTRANS from Section 3.2.1 over a sufficient range of velocities to span the atmospheric absorption signature. The CCF we adopt is defined as follows:

$$\mathrm{CCF}(v, \phi) = \sum_{\lambda_i = \lambda_{\min}}^{\lambda_{\max}} f(\lambda_i, v) F(\lambda_i, \phi), \qquad (13)$$

where $f(\lambda, v)$ is the template spectrum shifted by velocity v. Likewise, we cross-correlate our grid of RME/CLV models from Section 3.2.2 with the same Fe II template. Consequently, we obtain CCF maps analogous to Figure 2 that can be fit with the same MCMC procedure as given in Section 3.2.3.

Our cross-correlated flux maps display distinct features that are not attributable to the planet's atmospheric absorption track or the RME/CLV perturbations. In particular, our cross-correlation procedure reproduces the artifacts described in Hoeijmakers et al. (2019) as "stellar pulsations" in the HARPS-N data sets (see Figure 5). We model these artifacts as individual Gaussian features that have time-variable amplitudes, standard deviations, and centroids that gradually change across observations. We fit these features using nonlinear least-squares optimization and subtract the model from the observed cross-correlation flux map. Since these artifacts overlap in velocity-phase space with the atmospheric absorption track, we first subtract a preliminary fit of the planet's absorption and the Doppler shadow before removing the artifacts. See Figure 6 for observed and model CCF maps and the corresponding residuals for all four transmission spectroscopy data sets.

We also adopt a correlated noise model in our MCMC fitting procedure of the cross-correlated maps using the Gaussian process regression library george[10] (see middle row of

---
[10] https://george.readthedocs.io/en/latest/

Figure 6). Without this added component to the model, the parameter errors are notably underestimated. We assume a 2D Matérn-3/2 covariance kernel, resulting in one amplitude parameter and two length parameters in addition to our original model parameters to fit with MCMC. This additional step does not yield parameter posterior distributions that are statistically significantly different for the line-by-line analysis. For our cross-correlated data, however, including the Gaussian process to model the covariance structure of the data accurately captures the uncertainty from correlated noise.

3.3. Measuring Planet and Stellar Masses

As in Snellen et al. (2010), we treat the system as an SB2 to determine the planet and stellar masses. In previous sections, we demonstrated that (1) the absorption lines of the planet's atmosphere during transit capture the planet's orbital velocity, while (2) the out-of-transit observations can be deconvolved with a template stellar spectrum to retrieve the stellar orbital velocity. From conservation of momentum, we know that

$$m_p K_p = M_\star K_\star, \qquad (14)$$

where m_p and $M_\star$ are the masses and K_p and $K_\star$ are the RV semiamplitudes (or orbital velocity, in the case of a circular orbit) of the planet and star, respectively. Kepler's third law of orbital motion states

$$P^2 = \frac{4\pi^2}{G(M_\star + m_p)}(a_\star + a_p)^3. \qquad (15)$$

Assuming KELT-9 b is on a circular orbit based on an estimate of its circularization timescale (Borsa et al. 2019), we can relate the semimajor axes with observables we have previously measured, namely, the RV semiamplitudes of the planet (K_p) and star ($K_\star$), orbital inclination (i), and orbital period (P):

$$\frac{K_p}{\sin i} = \frac{2\pi a_p}{P}, \qquad (16)$$

$$\frac{K_\star}{\sin i} = \frac{2\pi a_\star}{P}, \qquad (17)$$

where a_p and $a_\star$ are the orbital semimajor axes of the planet and star, respectively. We can rewrite $M_\star$ in terms of m_p using Equation (14) and apply Equations (16) and (17) to recast the semimajor axes in terms of RV semiamplitudes and orbital period. This allows us to write our quantity of interest, m_p, in terms of purely empirical (and predominantly spectroscopic) observables. Upon doing so, we derive the following expression for planet mass:
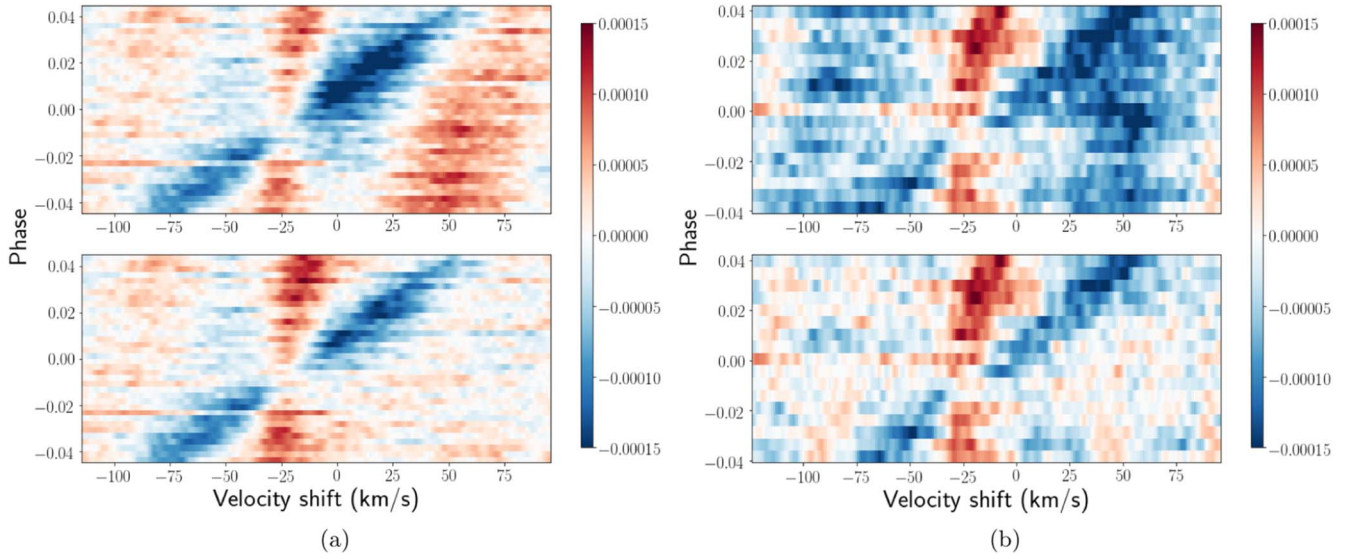
$$m_p = \frac{P K_\star}{2\pi G K_p}\left(\frac{K_p}{\sin i}\right)^3\left(1 + \frac{K_\star}{K_p}\right)^2. \qquad (18)$$

Applying this result to conservation of momentum (Equation (14)) yields the following expression for stellar mass:

$$M_\star = \frac{P}{2\pi G}\left(\frac{K_p}{\sin i}\right)^3\left(1 + \frac{K_\star}{K_p}\right)^2. \qquad (19)$$

Uncertainties on m_p and $M_\star$ are derived according to the linear propagation of errors (see the Appendix for the analytic expressions).

Figure 5. Cross-correlated flux maps before artifact correction in the top panel and after artifact correction in the bottom panel for the (a) PEPSI 2018 and (b) HARPS-N 2017 data sets.

4. Results

4.1. Summary of Findings

We present the revised planetary and stellar parameters resulting from our analysis in Table 3. Most notable is our measurement of the planetary mass, the first self-consistent, purely empirical measurement of KELT-9 b's dynamical mass, $2.17 \pm 0.56\,M_J$, by treating the system as an SB2. Another by-product of this analysis is the mass of the star, which we measure to be $2.11 \pm 0.78\,M_\odot$.

4.2. Comparison with Previous Literature

We now compare our measurement of the dynamical mass of KELT-9 b against previous literature (see Table 3). Throughout the following discussion, we define 1σ by adding in quadrature the errors from two studies of comparison for a parameter. Our measurement of $m_p = 2.17 \pm 0.56\,M_J$ agrees with Gaudi et al. (2017), Yan & Henning (2018), and Hoeijmakers et al. (2019).

The discrepancy in mass measurements across the literature can be largely attributed to the use of $K_\star$ given in Gaudi et al. (2017) and independent measurements of K_p (see Figure 7). Yan & Henning (2018) used $K_p = 268.7^{+6.2}_{-6.4}\,\mathrm{km\,s^{-1}}$ from their analysis of atmospheric dynamics using Hα as a tracer, as well as $K_\star = 0.276 \pm 0.079\,\mathrm{km\,s^{-1}}$ from the discovery paper; however, our measurement of $K_\star$ is nearly a factor of 1.2 ($\sim 0.42\sigma$ difference) less than that in the discovery paper. Hoeijmakers et al. (2019) uses a similar value of K_p as ours that agrees within the errors, which they obtained from fitting Fe II lines as well. Their procedure slightly differs from ours in regard to order of operations; instead of fitting their cross-correlated planet absorption track across all fully in-transit observations simultaneously for a given data set, they fit each observation with an independent Gaussian absorption feature and fit a single circular orbital solution to the individual planet RVs they obtained across both of their data sets. However, they used the planet mass from Gaudi et al. (2017) along with their value of K_p to revise the stellar mass but then updated the planet mass according to the value of $K_\star$ from Gaudi et al. (2017) and their revised stellar mass. Thus, their analysis is not self-consistent. Our analysis, on the other hand, is

self-consistent, because we obtain empirical values of K_p and $K_\star$ exclusively by applying the same routines and wavelength-consistent template line lists on all of the data we present in this work.

Studies of KELT-9 b's neutral iron emission such as Pino et al. (2020) and Kasper et al. (2021) obtain complementary constraints on K_p. In principle, one might expect these dayside measurements to disagree with our terminator measurements due to atmospheric circulation. However, the measurements of K_p from both Pino et al. (2020; displayed in Figure 7) and Kasper et al. (2021; not included in Figure 7 since this work did not consolidate their multiple constraints from different nights of observations into one measurement) agree within 1σ. This strengthens our claim that the planet's orbital parameters can be procured from the planet's transmission absorption signature without secondary effects from atmospheric processes like circulation or condensation.

We also find that our measurement of stellar mass agrees with Gaudi et al. (2017) and Hoeijmakers et al. (2019) but disagrees with Yan & Henning (2018) by 1.1σ.

Since stellar density is a direct observable from transit light curves (Seager & Mallén-Ornelas 2003), we can use our revised stellar mass measurement and empirical measurements of stellar radius from the literature to compute a stellar density and compare with the stellar density derived from the light curve as provided in Gaudi et al. (2017). The stellar radius provided in Gaudi et al. (2017) is directly constrained to be $R_\star = 2.17 \pm 0.33\,R_\odot$ from the Hipparcos parallax, effective temperature, bolometric flux of the star from integrating its SED, and interstellar extinction. Using our measurement of the host star's dynamical mass and $V = \frac{4}{3}\pi R_\star^3$ (assuming a spherical star) with the Gaudi et al. (2017) measurement for $R_\star$, we obtain a stellar density of $\rho_\star = 0.29 \pm 0.17\,\mathrm{g\,cm^{-3}}$, which is consistent with the direct measurement from the light curve in Gaudi et al. (2017) of $\rho_\star = 0.2702 \pm 0.0029\,\mathrm{g\,cm^{-3}}$. This suggests that our dynamical mass analysis agrees with independent metrics from previous studies. Note that the error on our empirical measurement of stellar density has nearly equivalent contributions from the error on the empirical radius
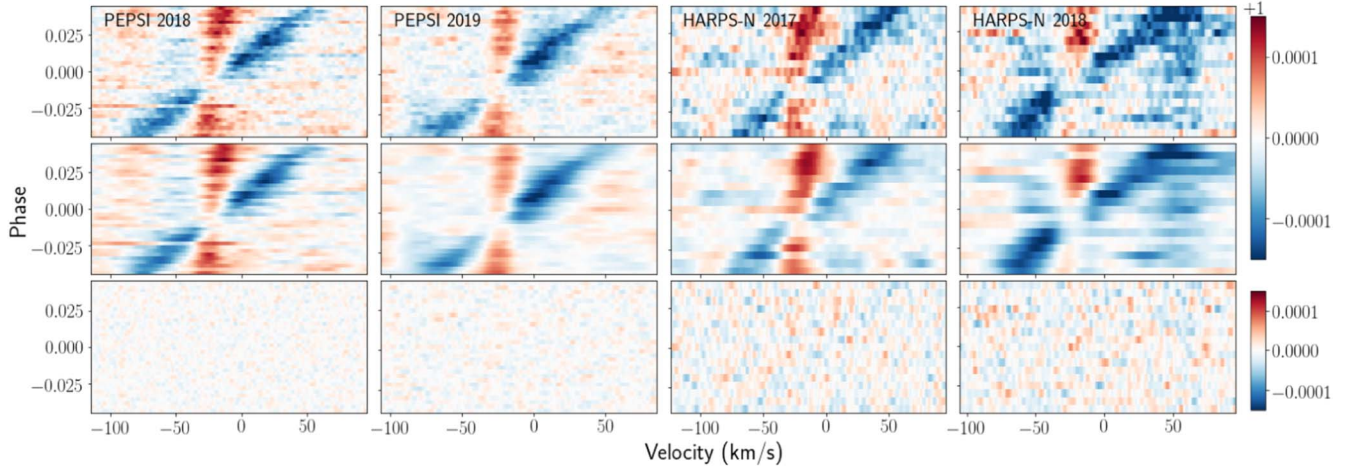
Figure 6. Same as Figure 3 except displaying CCF maps for each data set.

(∼55% of the stellar density error) and our empirical mass error (∼45% of the stellar density error).

We note that the spherical star assumption is not necessarily valid for fast rotators. Ahlers et al. (2020) went an additional step to account for effects from gravity darkening in their measurement of the stellar radius using TESS transit light curves of KELT-9 b. Gravity darkening is a phenomenon by which the effective temperature varies across a stellar surface due to a rapidly rotating star's oblateness perturbing the star's hydrostatic equilibrium near its equator (Ahlers et al. 2020). While Ahlers et al. (2020) did provide an equatorial radius and oblateness parameter that can, in principle, be combined with our mass measurement to recover a stellar density, we do not perform this step for comparison because the stellar equatorial radius they derived assumes a prior on the stellar mass based on Gaudi et al. (2017) of $M_* = 2.52^{+0.25}_{-0.20}\,M_\odot$, which differs from our measurement of $M_* = 2.11 \pm 0.78\,M_\odot$.

5. Discussion

5.1. Caveats to the Orbital Motion Model

The possibility of an eccentric orbit would undermine our measurement of K_p and, by extension, KELT-9 b's mass. Our model presumes that KELT-9 b and its host star obey circular orbital motion based on the planet's estimated circularization timescale (Borsa et al. 2019). Furthermore, we obtain an empirical constraint of $e\cos\omega = 4.77 \times 10^{-7} \pm 7.2 \times 10^{-5}$ from the ephemerides of the primary transit and secondary eclipse; the precision of this constraint is possible due to the inclusion of TESS observations in our global fit for the system ephemerides. With such a low value for $e\cos\omega$, it is unlikely that the planet's orbit is significantly eccentric enough to affect our empirical measurement of the planet's mass within the errors.

We also assume that the dominant effect of atmospheric dynamics on the planet's absorption signature between second and third contact is a constant RV offset due to dayside-to-nightside winds. Ehrenreich et al. (2020) showed that the wind component of WASP-76 b's atmospheric absorption signature changes from zero to ∼11 km s^{-1} over the course of the planet's transit. This would imply that our model of the planet's atmospheric absorption signature may not sufficiently capture the effect of KELT-9 b's atmospheric dynamics. However, we note that unlike Ehrenreich et al. (2020), our analysis does not
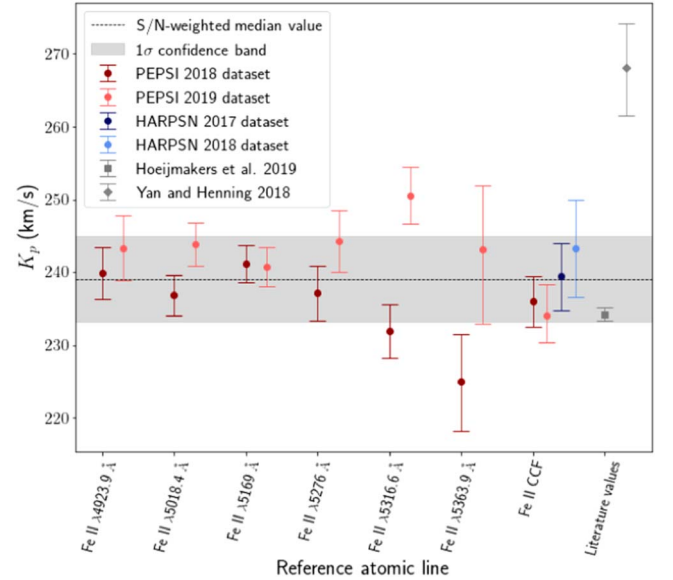
Figure 7. The K_p measurements from Fe II line-by-line and cross-correlation analysis with MCMC sampling errors.

include observations taken during ingress or egress in the procedure for fitting the orbital motion of the planet. Ingress and egress are expected to contribute the strongest asymmetries in the absorption signal due to eastward equatorial jets and rotation, yielding an additional redshift on the leading limb during ingress and a blueshift on the trailing limb during egress (assuming the planet's rotational axis and orbital axis are aligned); Ehrenreich et al. (2020) demonstrated this effect empirically. Since we exclude observations that capture a partial limb of the planet, these asymmetries should not manifest as strongly in our analysis.

Even if we were to include the entire transit in our analysis, the absorption signal during ingress and egress is not very strong in our observations. When we align all in-transit observations between first and fourth contact in the planet's rest frame and additionally remove the measured offset component for each data set, the absorption feature is visibly centered around 0 km s^{-1} over the course of the entire transit. This suggests that the wind speed does not appear to vary significantly over the course of the transit. Furthermore, the

asymmetry observed by Ehrenreich et al. (2020) shows a constant RV offset during the second half of the transit, which is where KELT-9 b's absorption signal is strongest and will contribute the most to our measured dayside-to-nightside wind measurement.

5.2. Complementary Constraints on System Parameters

Among its numerous significant attributes, one noteworthy characteristic of the KELT-9 system is that its physical properties are empirically overconstrained. In particular, additional empirical constraints are possible due to the gravity-darkening signature during the primary transit that originates from rotational flattening of the host star. The geometry of such systems introduces mathematical complexities that make quantitative analyses analytically intractable. Rather, numerical methods are required to obtain the system parameters; these are beyond the scope of this work. Therefore, we proceed to qualitatively describe the ways in which a complete, model-independent solution to the system parameters can be achieved.

The first method treats the system as an SB2, as done in this work. We have determined the masses of the system from spectroscopic observables in this work by treating the KELT-9 system as an eclipsing SB2; thus, all of the orbital elements ($K_\star$, K_p, $a_\star$, a_p, etc.) of the system are known. Furthermore, one can apply the assumption that the orbit is circular to get the stellar and planetary semimajor axes $a_\star$ and a_p, respectively. Determining the radii of the host star and planet is complicated somewhat by the fact that the star is oblate and gravity-darkened. However, the photometric gravity-darkening signature during the primary transit (as presented in Ahlers et al. 2020) uniquely constrains the inclination of the stellar rotational axis, as well as the stellar oblateness parameter. These two parameters then completely specify the geometry of the planet's transit across the oblate stellar disk, taking into account the planet's orbital inclination (angular offset along the line of sight between the plane of the planet's orbit and the plane of the sky), stellar inclination (angular offset along the line of sight between the stellar rotation axis and the plane of the sky), and spin–orbit obliquity (angular offset in the plane of the sky between the stellar rotation axis and the planet's orbital axis). The chord transited by the planet is related to the equatorial stellar radius by these angular quantities and the oblateness of the star. From this, the equatorial stellar radius can be related to the orbital semimajor axis by the FWHM transit duration and orbital period. The planet's radius is consequently obtained from the ratio of the planet radius to the stellar equatorial radius provided in Ahlers et al. (2020). Thus, a complete mass–radius solution to the KELT-9 system can be obtained.

A second approach is to use just the host star RVs in combination with an empirical stellar radius from an SED and parallax. The latter part of this approach is provided in Gaudi & Winn (2007) using KELT-9's Hipparcos parallax, yielding $R_\star = 2.17 \pm 0.33\,R_\odot$. This empirical radius is more appropriately thought of as an effective radius, since it assumes a spherical star with a uniformly illuminated sky-projected disk. This empirical radius can be translated into a measurement of the true stellar equatorial radius by determining the equatorial radius (given the oblateness parameter from Ahlers 2016) that yields an equivalent integrated disk flux to the spherical case. Numerically integrating the oblate star disk flux as done in

Ahlers (2016) requires accounting for (1) the star's longitudinal variation in flux from limb darkening (Equation (4) of Ahlers 2016), (2) latitudinal variation in flux from gravity darkening (Equation (2) of Ahlers 2016), and (3) inclination of the stellar rotational axis, which affects both the sky-projected disk shape of the oblate star and the range of latitudes visible along the line of sight (relevant for the latitude dependence of the gravity-darkening profile). As before, the planet's radius is deduced from the ratio of planet radius to stellar equatorial radius given in Ahlers et al. (2020). The stellar mass can be determined from the stellar radial parameters in combination with stellar density, a transit observable as given in Seager & Mallén-Ornelas (2003). The relation for stellar density will require modifications for the geometry of an oblate and inclined spheroid star transited by a planet on an inclined and oblique circular orbit. These nuances directly affect the relations between transit observables, i.e., depth and duration, and the system parameters of interest, i.e., $a/R_{\star,\mathrm{eq}}$ and $\rho_\star$. Lastly, the planet mass can be related to the stellar mass by the stellar RV semiamplitude as given in Equation (9) of Hoeijmakers et al. (2019) for the complete solution to the system. A revised measurement of the empirical stellar radius with a Gaia parallax would significantly improve the precision of this constraint.

The third approach combines the single-lined spectroscopy measurement of $K_\star$ with the photometric gravity-darkening signature during primary transit, which provides constraints on stellar surface gravity. Since the host star is an oblate spheroid, the surface gravity varies spatially, as given by Equation (10) of Barnes (2009). The transit signature maps the stellar surface brightness as the planet crosses the stellar disk. For a given $R_\star$ and external constraint on $v \sin i_\star$, one can uniquely determine the limb-darkening coefficients, oblateness, stellar inclination, orbital inclination, and spin–orbit obliquity, as done in Ahlers et al. (2020). For a given stellar equatorial radius, the system can be uniquely solved. Stellar mass is related to stellar radius using the stellar density, a transit observable (taking into account the nuances in the case of an oblate star, as described above). Then, as before, the planet radius can be obtained from the planet-to-star radius ratio from the gravity-darkening transit signature, and the planet mass comes from Equation (9) of Hoeijmakers et al. (2019). The only missing component to solve the system is the stellar radius. Ahlers et al. (2020) used a gravity-darkening correction on the SED from Gaudi et al. (2017), similar to our description in the second approach. To distinguish this third approach from the second, we note that the stellar equatorial radius is related to the gravity-darkening exponent β and stellar inclination by plugging Equation (10) of Barnes (2009) into Equation (9) of the same work. These quantities are not degenerate because their effects are not scaled versions of each other. Thus, it is possible to determine a unique solution for the equatorial radius based on the shape of the transit light curve and thus all of the other geometric parameters (stellar oblateness, inclination, spin–orbit obliquity, limb-darkening coefficients, and the gravity-darkening exponent).

The fourth and final approach we present combines the single-lined spectroscopy measurement of $K_\star$ with stellar surface gravity as measured by the broadening of the stellar absorption lines seen in high-resolution spectra. This measurement of $\log(g_\star)$ does not account for the fact that surface gravity varies spatially across the surface of an oblate star.

Instead, it serves more as an effective surface gravity assuming a spherical star. Under this assumption, Section 2.3.1 of Stevens et al. (2018) presents a derivation of the system parameters from the spectroscopic stellar RV semiamplitude and spectroscopic stellar surface gravity. This constraint is the weakest because it does not account for the oblate geometry of the star. Additionally, spectroscopically determining the surface gravity of hot, rapid rotators is challenging, since their absorption features are dominated by rotational broadening.

We hope these four approaches guide future follow-up work to cross-validate and tighten constraints on the KELT-9 system and other transiting two-body systems in which the primary is a rapid rotator.

5.3. Independent Metrics of Mass in the Literature

With sufficient photometric precision, the BEaming, Ellipsoidal, and Reflection algorithm (Faigler & Mazeh 2011) enables the detection of short-period massive planets, both transiting and nontransiting. This technique encompasses three distinct photometric signatures, of which two (Doppler beaming and ellipsoidal variations) depend on the mass of the planet. We provide order-of-magnitude estimates of these signals based on our revised mass constraints.

Doppler beaming is the periodic variation in flux due to the orbital motion of a star hosting a companion (Loeb & Gaudi 2003). The fractional amplitude in flux modulations is given in Loeb & Gaudi (2003) as

$$\frac{\Delta F}{F_0} = \frac{3 - \alpha_{\mathrm{beam}}}{c} K_\star, \tag{20}$$

where α_{beam} is the power-law exponent of the emitted flux from the source star as a function of frequency. We can estimate the α_{beam} of a blackbody source with an effective temperature T_{eff} according to Equation (3) in Loeb & Gaudi (2003) as $\alpha_{\mathrm{beam}}(\nu) \approx \frac{e^x(3-x)-3}{e^x-1}$, where $x = \frac{h\nu}{kT_{\mathrm{eff}}}$. Adopting the frequency corresponding to the V-band wavelength of 551 nm as a representative frequency, we obtain a Doppler beaming signal on the order of $\frac{\Delta F}{F_0} = 2.17$ ppm. This estimated signal falls far below the photometric precision of present-day instruments like TESS to be discernible.

Ellipsoidal variations are flux perturbations that arise as a consequence of tidal effects induced by a companion. Equation (2) of Faigler & Mazeh (2011) estimates the ellipsoidal variations of amplitudes

$$A_{\mathrm{ellip}} = \alpha_{\mathrm{ellip}} \frac{m_{\mathrm{p}} \sin i_{\mathrm{orbit}}}{M_\star} \left(\frac{R_\star}{a}\right)^3 \sin i_{\mathrm{orbit}}, \tag{21}$$

where α_{ellip} is defined in Equation (4) of Faigler & Mazeh (2011) as

$$\alpha_{\mathrm{ellip}} \approx 0.15 \frac{(15 + u)(1 + g)}{3 - u}. \tag{22}$$

The parameter u is the linear limb-darkening coefficient of the star, which we take to be $u = 0.3356$ based on Claret (2017). We adopt edge cases of $g = 0.3$ and 1 for the gravity-darkening coefficient (not to be mistaken for the gravity-darkening exponent from Ahlers et al. 2020), as suggested in Faigler & Mazeh (2011). The ratio $\frac{R_\star}{a}$ is a direct observable from transit light curves; we use $\frac{a}{R_\star} = 3.153$ from Gaudi et al. (2017). The

resulting estimate of the ellipsoidal variations signal based on our mass ratio ranges between 35.0 and 53.8 ppm.

Wong et al. (2020) presented photometric harmonics in the phase curve of the KELT-9 system by phase-folding TESS light curves and binning at 30 minute intervals. They measured periodic variations attributable to ellipsoidal variations with an amplitude of 39.6 ± 4.5 ppm. This measurement is within the range of the ellipsoidal variation signal amplitudes we estimate based on our revised masses of the system. In fact, it is marginally easier to explain Wong et al.'s (2020) measurement with our planet–star mass ratio than with the original value in Gaudi et al. (2017), which yields ellipsoidal variation signal amplitudes between 38.9 and 60.0 ppm for the same range of values for β. Note that numerous uncertainties play into our estimate of ellipsoidal variations, such as the uncertainty of the limb- and gravity-darkening coefficients of this particular star. In particular, the metallicity and evolutionary effects on the limb-darkening coefficient are stronger after the onset of convection ($\log T_{\mathrm{eff}} > 3.9$; Claret 2017). Furthermore, the star is significantly distorted by rotation, and the planet's orbit is nearly orthogonal to this distortion. This geometry limits the gravitational distortion of the star by the companion planet and weakens the signal from ellipsoidal variations.

5.4. Consequences for Atmospheric Escape

As the hottest planet known to date, KELT-9 b is a unique target for studying the hydrodynamic escape of planetary atmospheres driven by extreme stellar irradiation (Fossati et al. 2018; García Muñoz & Schneider 2019; Krenn et al. 2021). Observations of atmospheric loss on KELT-9 b use light-element tracers such as Balmer lines (Yan & Henning 2018; Cauley et al. 2019; Wyttenbach et al. 2020) and Mg I (Cauley et al. 2019) to probe mass-loss rates according to empirically validated species densities and a slew of assumptions surrounding elemental abundances and equilibrium conditions. Notably, these studies generally assume thermodynamic and ionization equilibrium, as well as solar abundances of species; the former may be discounted by NLTE studies of KELT-9 b's upper atmosphere (García Muñoz & Schneider 2019; Wyttenbach et al. 2020; Fossati et al. 2021), while the latter may be invalidated by recent work on atmospheric retrieval of HJs (Giacobbe et al. 2021).

We summarize the state of the field to date regarding the mass-loss rate of KELT-9 b. Gaudi et al. (2017) provided an initial estimate of KELT-9 b's mass-loss rate between 10^{10} and 10^{13} g s^{-1} based on the equation for the energy-limited mass-loss rate provided in Equation (22) of Murray-Clay et al. (2009), which scales inversely with the mass of the planet. Yan & Henning (2018) empirically constrained KELT-9 b's mass-loss rate by identifying an excess in Hα absorption depth relative to the photometric transit depth in the continuum. By estimating (1) the number density of hydrogen from model fits to the Hα line profile (these models depend on planetary parameters, most notably planet mass) and (2) the contribution from the altitude regime of the planet where Hα can energetically escape beyond the planet's Roche lobe, Yan & Henning (2018) estimated a mass-loss rate of $\dot{M} \sim 10^{12}$ g s^{-1}. Cauley et al. (2019) corroborated this measurement within an order of magnitude, estimating $\dot{M} \sim 1 \times 10^{12}$ g s^{-1} when using Mg I as a tracer and $\dot{M} \sim 3 \times 10^{12}$ g s^{-1} from Balmer line analysis. Wyttenbach et al. (2020) reported $\dot{M} \sim 10^{12.8 \pm 0.3}$ g s^{-1} from Balmer line analysis as well.

Reconciling observations of KELT-9 b's atmospheric escape with theory currently faces unresolved challenges. HJ atmospheric escape is typically modeled as hydrodynamic escape due to heating from Lyman continuum absorption in the X-ray and extreme-ultraviolet (XUV). Fossati et al. (2018) notes that ionizing XUV fluxes in the wavelength regime relevant to heating (and thus escape) are weaker in hotter intermediate mass stars, such as the stellar host of the KELT-9 system, than their cooler (~8000–8500 K) counterparts, such as the host of another UHJ WASP-33 b. XUV flux is driven by coronal heating, which is related to stellar magnetic activity. A convective envelope is necessary for the interactions that generate magnetic activity. The surface convective zone vanishes in hotter stars and consequently they emit less XUV flux. Fossati et al. (2018) estimate KELT-9 b's mass-loss rate is $\sim10^{10}-10^{11}$ g s^{-1} by accounting for the heating efficiency of XUV flux from the KELT-9 host star. Their estimated Hα transit depth of 0.7% does not agree with the observed 1.8% in Yan et al. (2017). They propose that one way of bridging this gap is by adopting a planetary mass on the lower end of the 1σ range provided in Gaudi et al. (2017; $M_{\rm p} = 2.88 \pm 0.84\,M_{\rm J}$). As previously noted, $\dot{M}$ scales inversely with planet mass in the most simplified energy-limited case, which balances gravitational potential and thermal heating from the host star's X-ray and extreme-UV (EUV) radiation. This would bring the planetary mass required to explain observations of KELT-9 b's atmospheric loss in closer agreement with our revised empirical mass. We estimate that our revised mass increases the estimated energy-limited mass-loss rate (see Fossati et al. 2018 for a discussion of this estimate for KELT-9 b and its nuances) by ∼33%. Note that recent work by Krenn et al. (2021) comparing the energy-limited approximation against hydrodynamic simulations of atmospheric escape shows that the energy-limited approximation is not suited for estimating UHJ mass-loss rates (or planets in extreme temperature or mass regimes in general; UHJs satisfy both of these conditions).

García Muñoz & Schneider (2019) expands upon the implications of Fossati et al. 2018 by proposing that Balmer continuum absorption in the near-ultraviolet is the dominant source of heating in KELT-9 b's atmosphere. However, their models best match observations of KELT-9 b's Hα absorption when adopting a planet mass between 0.80–1.20 $M_{\rm J}$. This is incompatible with our revised mass.

6. Conclusion

We have presented the analysis of spectroscopic data of KELT-9 b in the context of an eclipsing SB2. This has enabled us to directly and empirically obtain the dynamical mass of KELT-9 b and its host star. Using multiepoch spectroscopic observations of the system, we find that the dynamical mass of the planet is $m_{\rm p} = 2.17 \pm 0.56\,M_{\rm J}$, and the star is $M_{\star} = 2.11 \pm 0.78\,M_{\odot}$. Our planet mass measurement generally agrees with previous literature (Gaudi et al. 2017; Hoeijmakers et al. 2019). We also obtain a purely empirical measurement of stellar density, a direct observable from transit light curves, that agrees with the value in the discovery paper; this suggests that our analysis is trustworthy. Our methodology can be applied to many HJ systems, thereby enabling the direct and empirical measurement of their planets and host stars.

We note that the KELT-9 system is empirically overconstrained due to the unique geometric information provided by the in-transit gravity-darkening signature of rapid-rotator

systems. We present a framework for obtaining a complete solution to the system parameters in three purely observational ways.

An order-of-magnitude estimate shows that this revised planetary mass is large enough to induce ellipsoidal variations observable with TESS phase curves of the KELT-9 system. Furthermore, this result is especially crucial for studies of atmospheric escape, which depend on mass for empirical measurement and theoretical modeling; as of now, the high levels of atmospheric escape seen on KELT-9 b have not been reconciled with its high mass. Our purely empirical confirmation of the planet's mass motivates further exploration of this conundrum surrounding the substantial mass loss on KELT-9 b.

Appendix
Error Propagation of Stellar and Planetary Mass from RV Observables

We apply linear propagation of errors to recover the following expression for the propagated uncertainty of the planet mass:

$$\delta m_{\rm p} = \left[\left(\frac{\partial m_{\rm p}}{\partial P} \right)^2 \delta P^2 + \left(\frac{\partial m_{\rm p}}{\partial i} \right)^2 \delta i^2 \right.$$
$$\left. + \left(\frac{\partial m_{\rm p}}{\partial K_{\rm p}} \right)^2 \delta K_{\rm p}^2 + \left(\frac{\partial m_{\rm p}}{\partial K_{\star}} \right)^2 \delta K_{\star}^2 \right]^{1/2}.$$

We present the analytic form of each partial derivative term in Equation (6) below:

$$\frac{\partial m_{\mathrm{p}}}{\partial P} = \frac{K_\star (K_{\mathrm{p}} + K_\star)^2}{2\pi G \sin^3 i},$$

$$\frac{\partial m_{\mathrm{p}}}{\partial i} = \frac{-3K_\star (K_{\mathrm{p}} + K_\star)^2 P \cos i}{2\pi G \sin^2 i},$$

$$\frac{\partial m_{\mathrm{p}}}{\partial K_{\mathrm{p}}} = \frac{K_\star (K_{\mathrm{p}} + K_\star) P}{\pi G \sin^3 i},$$

$$\frac{\partial m_{\mathrm{p}}}{\partial K_\star} = \frac{(K_{\mathrm{p}} + K_\star)(K_{\mathrm{p}} + 3K_\star) P}{2\pi G \sin^3 i}.$$

Analogously, the propagated stellar mass uncertainty is

$$\delta M_\star = \left[\left(\frac{\partial M_\star}{\partial P}\right)^2 \delta P^2 + \left(\frac{\partial M_\star}{\partial i}\right)^2 \delta i^2 \right.$$
$$\left. + \left(\frac{\partial M_\star}{\partial K_{\mathrm{p}}}\right)^2 \delta K_{\mathrm{p}}^2 + \left(\frac{\partial M_\star}{\partial K_\star}\right)^2 \delta K_\star^2 \right]^{1/2},$$

with partial derivative terms of the form

$$\frac{\partial m_{\mathrm{p}}}{\partial P} = \frac{K_{\mathrm{p}}(K_{\mathrm{p}} + K_\star)^2}{2\pi G \sin^3 i},$$

$$\frac{\partial m_{\mathrm{p}}}{\partial i} = \frac{-3K_{\mathrm{p}}(K_{\mathrm{p}} + K_\star)^2 P \cos i}{2\pi G \sin^2 i},$$

$$\frac{\partial m_{\mathrm{p}}}{\partial K_{\mathrm{p}}} = \frac{(K_{\mathrm{p}} + K_\star)(3K_{\mathrm{p}} + K_\star) P}{2\pi G \sin^3 i},$$

$$\frac{\partial m_{\mathrm{p}}}{\partial K_\star} = \frac{K_{\mathrm{p}}(K_{\mathrm{p}} + K_\star) P}{\pi G \sin^3 i}.$$

ORCID iDs

Anusha Pai Asnodkar ⓘ https://orcid.org/0000-0002-8823-8237
Ji Wang (王吉) ⓘ https://orcid.org/0000-0002-4361-8885
B. Scott Gaudi ⓘ https://orcid.org/0000-0003-0395-9869
P. Wilson Cauley ⓘ https://orcid.org/0000-0001-9207-0564
Jason D. Eastman ⓘ https://orcid.org/0000-0003-3773-5142
Ilya Ilyin ⓘ https://orcid.org/0000-0002-0551-046X
Klaus Strassmeier ⓘ https://orcid.org/0000-0002-6192-6494
Thomas Beatty ⓘ https://orcid.org/0000-0002-9539-4203

References

Ahlers, J. P. 2016, ApJ, 832, 93
Ahlers, J. P., Johnson, M. C., Stassun, K. G., et al. 2020, AJ, 160, 4
Andersen, J. 1991, A&ARv, 3, 91
Barnes, J. W. 2009, ApJ, 705, 683
Borsa, F., Rainer, M., Bonomo, A. S., et al. 2019, A&A, 631, A34
Casasayas-Barris, N., Pallé, E., Yan, F., et al. 2020, A&A, 640, C6
Cauley, P. W., Shkolnik, E. L., Ilyin, I., et al. 2019, AJ, 157, 69
Choi, J., Dotter, A., Conroy, C., et al. 2016, ApJ, 823, 102
Claret, A. 2017, A&A, 600, A30

Collier Cameron, A., Bruce, V. A., Miller, G. R. M., Triaud, A. H. M. J., & Queloz, D. 2010, MNRAS, 403, 151
Donatelli, M., & Reichel, L. 2014, JCoAM, 272, 334
Donati, J. F., Semel, M., Carter, B. D., Rees, D. E., & Collier Cameron, A. 1997, MNRAS, 291, 658
Dotter, A. 2016, ApJS, 222, 8
Duck, A., Gaudi, B. S., Rodriguez, J., & Eastman, J. 2021, in preparation
Eastman, J. 2012, Time Utilities, Astrophysics Source Code Library, ascl:1206.012
Eastman, J., Siverd, R., & Gaudi, B. S. 2010, PASP, 122, 935
Eastman, J. D., Rodriguez, J. E., Agol, E., et al. 2019, arXiv:1907.09480
Ehrenreich, D., Lovis, C., Allart, R., et al. 2020, Natur, 580, 597
Erkaev, N. V., Kulikov, Y. N., Lammer, H., et al. 2007, A&A, 472, 329
Faigler, S., & Mazeh, T. 2011, MNRAS, 415, 3921
Foreman-Mackey, D., Hogg, D. W., Lang, D., & Goodman, J. 2013, PASP, 125, 306
Fossati, L., Koskinen, T., Lothringer, J. D., et al. 2018, ApJ, 868, L30
Fossati, L., Young, M. E., Shulyak, D., et al. 2021, A&A, 653, A52
Gaia Collaboration, Brown, A. G. A., Vallenari, A., et al. 2021, A&A, 649, A1
Gaia Collaboration, Prusti, T., de Bruijne, J. H. J., et al. 2016, A&A, 595, A1
García Muñoz, A., & Schneider, P. C. 2019, ApJL, 884, L43
Gaudi, B. S., Stassun, K. G., Collins, K. A., et al. 2017, Natur, 546, 514
Gaudi, B. S., & Winn, J. N. 2007, ApJ, 655, 550
Giacobbe, P., Brogi, M., Gandhi, S., et al. 2021, Natur, 592, 205
Gray, D. F. 2005, The Observation and Analysis of Stellar Photospheres (3rd edn.; Cambridge: Cambridge Univ. Press)
Harmanec, P. 1988, BAICz, 39, 329
Hoeijmakers, H. J., Ehrenreich, D., Kitzmann, D., et al. 2019, A&A, 627, A165
Kasper, D., Bean, J. L., Line, M. R., et al. 2021, ApJL, 921, L18
Kochukhov, O., Makaganiuk, V., & Piskunov, N. 2010, A&A, 524, A5
Krenn, A. F., Fossati, L., Kubyshkina, D., & Lammer, H. 2021, A&A, 650, A94
Kubyshkina, D., Fossati, L., Erkaev, N. V., et al. 2018, ApJL, 866, L18
Loeb, A., & Gaudi, B. S. 2003, ApJL, 588, L117
McLaughlin, D. B. 1924, ApJ, 60, 22
Mollière, P., Wardenier, J. P., van Boekel, R., et al. 2019, A&A, 627, A67
Murray-Clay, R. A., Chiang, E. I., & Murray, N. 2009, ApJ, 693, 23
Ohta, Y., Taruya, A., & Suto, Y. 2005, ApJ, 622, 1118
Pakhomov, Y., Piskunov, N., & Ryabchikova, T. 2017, in ASP Conf. Ser. 510, Stars: From Collapse to Collapse, ed. Y. Y. Balega (San Francisco, CA: ASP), 518
Palme, H., Lodders, K., & Jones, A. 2014, in Solar System Abundances of the Elements, ed. A. M. Davis, Vol. 2 (Amsterdam: Elsevier), 15
Pino, L., Désert, J.-M., Brogi, M., et al. 2020, ApJ, 894, L27
Popper, D. M. 1980, ARA&A, 18, 115
Queloz, D., Eggenberger, A., Mayor, M., et al. 2000, A&A, 359, L13
Ricker, G. R., Winn, J. N., Vanderspek, R., et al. 2014, JATIS, 1, 014003
Rossiter, R. A. 1924, ApJ, 60, 15
Sanz-Forcada, J., Micela, G., Ribas, I., et al. 2011, A&A, 532, A6
Seager, S., & Mallén-Ornelas, G. 2003, ApJ, 585, 1038
Snellen, I. A. G., de Kok, R. J., de Mooij, E. J. W., & Albrecht, S. 2010, Natur, 465, 1049
Stenflo, J. O. 2015, A&A, 573, A74
Stevens, D. J., Gaudi, B. S., & Stassun, K. G. 2018, ApJ, 862, 53
Strassmeier, K. G., Ilyin, I., Järvinen, A., et al. 2015, AN, 336, 324
Tayar, J., Claytor, Z. R., Huber, D., & van Saders, J. 2020, arXiv:2012.07957
Torres, G., Andersen, J., & Giménez, A. 2010, A&ARv, 18, 67
Valenti, J. A., & Piskunov, N. 1996, A&AS, 118, 595
Valenti, J. A., & Piskunov, N. 2012, SME: Spectroscopy Made Easy, Astrophysics Source Code Library, ascl:1202.013
Virtanen, P., Gommers, R., Oliphant, T. E., et al. 2020, NatMe, 17, 261
Wang, J., Prato, L., & Mawet, D. 2017, ApJ, 838, 35
Wong, I., Shporer, A., Kitzmann, D., et al. 2020, AJ, 160, 88
Wyttenbach, A., Mollière, P., Ehrenreich, D., et al. 2020, A&A, 638, A87
Yan, F., Fosbury, R. A. E., Petr-Gotzens, M. G., Zhao, G., & Pallé, E. 2015, A&A, 574, A94
Yan, F., & Henning, T. 2018, NatAs, 2, 714
Yan, F., Pallé, E., Fosbury, R. A. E., Petr-Gotzens, M. G., & Henning, T. 2017, A&A, 603, A73